Journal of Cranio-Maxillo-Facial Surgery 47 (2019) 1943–1951

Contents lists available at ScienceDirect

Journal of Cranio-Maxillo-Facial Surgery

journal homepage: www.jcmfs.com

Endoscopically assisted computer-guided repair of internal orbital floor fractures: an updated protocol for minimally invasive management

Alessandro Tel [a], Salvatore Sembronio [a], Fabio Costa [a], Alessandro Scipio Stenico [a], Daniele Bagatto [b], Serena D'Agostini [b], Massimo Robiony [a, *]

[a] Maxillofacial Surgery Department, Academic Hospital of Udine, Department of Medicine, University of Udine, Italy
[b] Neuroradiology Department, Academic Hospital of Udine, Department of Medicine, University of Udine, Italy

ARTICLE INFO

Article history:
Paper received 26 July 2019
Accepted 18 November 2019
Available online 27 November 2019

Keywords:
Virtual surgical planning
Accuracy
Orbital fracture
Endoscopy
3D printing
Facial care project

ABSTRACT

Background: Performing accurate anatomical reconstruction is a challenging task in the treatment of internal orbital floor fractures. Compared with traditional transcutaneous incisions, endoscopic transmaxillary approaches have the advantage of avoiding complications related to external scars, and provide direct access to the orbital floor. Autogenous bone provides the ideal material for defect reconstruction, but determination of the correct size and shape of the graft is crucial for a stable support. This study introduces a new protocol for the treatment of internal orbital floor fractures that combines endoscopy, virtual reality, and 3D printing. The authors also investigated the impact of computer-aided surgery (CAS) on the overall accuracy of reconstruction in aiming to achieve the triple objective of restoring anatomy, volume, and function.

Materials and methods: Fourteen patients with orbital floor fractures were recruited for this study. High-resolution CT scans provided appropriate imaging for detailed orbital floor defect visualization. A virtual reconstruction of the orbital floor defect was developed and a 3D printed template was fabricated to provide intraoperative guidance in the graft harvesting phase, according to the orbital defect. Virtual analyses were conducted to evaluate the accuracy of reconstruction both in terms of graft size and graft orientation.

Results: Postoperative CT scans showed that in all cases orbital floor reconstruction was successfully performed, resulting in restoration of the correct globe position. No intraoperative complications occurred. Correspondence of graft size was evaluated using color-coded maps and RMSE, while comparison of angular measurements allowed the authors to relate simulated and actual reconstruction.

Conclusions: Orbital floor reconstruction performed via transmaxillary endoscopy is a safe technique, which allows for detailed visualization of the fracture rim, avoids external scars, and permits an easier reduction of the prolapsed orbital content into the overlying orbital cavity. Virtual planning plays an important role in defining the appropriate geometry of the bone graft and establishing the optimal reconstruction strategy. Our preliminary results indicate that virtual planning and 3D printing should become part of an integrated protocol for the endoscopic treatment of orbital floor fractures.

1. Introduction

Pure orbital blowout fractures, also defined as internal orbital floor fractures, are confined within the internal orbital wall, with no involvement of the orbital rim or other facial bones. Orbital fractures involving the internal orbital floor often occur in patients who experience blunt trauma to the face and skull (Ahmad Nasir S et al., 2018; Beigi et al., 2014).

The bone defect results in a prolapse of orbital content into the paranasal sinuses and the entrapment of extraocular muscles, which might cause long-term functional impairment.

Patients generally present with diplopia, enophthalmos, vertical dystopia, paresthesia of the infraorbital nerve, and soft tissue

* Corresponding author. Head of Maxillofacial Surgery Department, Academic Hospital of Udine, Department of Medicine, University of Udine, P.le S. Maria della Misericordia 1, 33100, Udine, Italy.
E-mail address: massimo.robiony@uniud.it (M. Robiony).

https://doi.org/10.1016/j.jcms.2019.11.005
1010-5182/

incarceration or entrapment, leading to restriction of ocular movements (Mazock et al., 2004).

The surgical treatment of orbital floor fractures continues to be discussed and remains controversial. Several approaches have been used to reconstruct orbital wall defects, including inferior eyelid incision, conjunctival incision, and endoscopic approaches (Sanno et al., 2003).

Lower eyelid incisions have an inherent risk of ectropion, scleral show, entropion, canthal malposition, and lid edema. Additionally, fractures involving the posterior orbital floor may be difficult to visualize using traditional lower eyelid approaches, due to the posterior angulation of the orbital floor (Kwon et al., 2008).

More recently, orbital floor fractures have been treated using endoscopy, which aims to minimize complications typical of lower eyelid approaches and reduce recovery times. The use of the endoscope in orbital fractures allows for a clear observation of the fracture site, especially the posterior orbital floor.

The endoscopic transantral insertion of maxillary bone grafts through the floor defect into the orbit is an effective technique that avoids injuries to the lower eyelid, carries minimal donor site morbidity, avoids external skin incisions, and provides an optimal support function for the globe (Persons and Wong, 2002).

Conversely, in more extended defects, reconstruction performed only with the endoscope might be difficult and require additional techniques, including a combination of inferior eyelid incision and endoscopy (Farwell and Strong, 2007; Strong et al., 2004). Especially when insertion of implants is considered, lower eyelid approaches allow the surgeon to easily introduce implants while endoscopy provides improved visualization of the posterior region (Nahlieli et al., 2007). However, unlike with implants, it is often challenging to achieve stable endoscopic positioning of the bone graft onto the orbital floor defect, because the graft dimensions must adapt precisely to the fracture rim. In cases when a larger defect has to be reconstructed using a bone autograft, harvesting an optimally sized graft is essential.

In recent years, CAD (computer-aided design) has allowed the simulation of many different surgical situations, and the creation of personalized treatment plans. 3D printing (CAM — computer-aided manufacturing) has led to the production of prototype surgical templates that allow virtual planning to be translated into real operative coordinates.

This study presents an updated protocol based on virtual surgical planning and 3D printing for the endoscopic treatment of internal orbital floor fractures. A defect-driven protocol for the reconstruction of internal orbital floor fractures is combined with the use of virtual reality in the preoperative study of the patient. Elements such as the orientation and size of the bone graft are emphasized and re-evaluated in the postoperative phase to verify the accuracy of reconstruction.

2. Material and methods

2.1. Patients

Fourteen patients with internal orbital floor fractures were recruited for this study in the Maxillofacial Department, Academic Hospital of Udine, between June 2017 and April 2018. Written informed consent was obtained after patients were advised about the risks and benefits relating to the treatment options. Patients' characteristics are summarized in Table 1. Causes of injury were classified into four groups: assaults (42.9%), sport accidents (28.6%), falling from heights (14.9%), and car accidents (14.9%).

The time elapsed before surgical intervention allowed us to subdivide patients into two groups: patients undergoing early surgical intervention (79%), namely within 14 days of the trauma (Damgaard et al., 2016), and patients who underwent late surgical intervention (21%).

Table 1
Characteristics of patients.

Patient	Age	Sex	Cause of injury	Jaquiery's class
1	38	M	Assault	II
2	22	M	Sport accident	II
3	25	M	Sport accident	II
4	54	M	Assault	III
5	61	M	Assault	III
6	36	F	Car accident	III
7	30	M	Sport accident	II
8	78	F	Falling from height	II
9	65	M	Assault	III
10	81	M	Falling from height	III
11	20	M	Assault	III
12	46	M	Assault	II
13	52	F	Car accident	III
14	32	M	Sport accident	II

All patients underwent preoperative clinical examination, including evaluation of visual acuity, eye movements, exophthalmometry, and the Hess Lancaster screen test.

Indications for the surgical exploration of the orbital floor included the following signs and symptoms: persistent, vertical and disabling diplopia 1 week after trauma; enophthalmos greater than 2 mm; vertical dystopia; CT evidence of herniation of endo-orbital content; and a positive forced duction test. The magnitude of the orbital defect was determined according to the classes originally defined by Jaquiéry (Jaquiéry et al., 2007) (Table 2). Patients presenting with class I, class IV, and class V defects were excluded from our study.

After surgery, all patients underwent a CT scan at 48 h postoperatively. Postoperative follow-up for each patient was obtained at 1 month, 2 months, and 6 months, through clinical examination. Monitored complications included persistent diplopia, vertical dystopia, enophthalmos, graft resorption, and maxillary sinusitis.

The protocol introduced by this study is schematically represented in Fig. 1.

2.2. Image acquisition and virtual surgical planning

All patients underwent CT examination using a 64-row scanner (LightSpeed VCT 64; General Electric, Milwaukee, USA) in the same Neuroradiology Unit of the Diagnostic Imaging Department. The main CT scan technical parameters were as follows: 100 kV, 120 mA, noise index 7, rotation time 1.0 s, acquisition matrix 768 × 768 pixels, slice thickness 0.625 mm.

Raw DICOM data were processed using the software Mimics 21 (Materialise, Leuven, BE) and high-resolution 3D meshes were created, providing a three-dimensional representation of the internal orbital fractures. Based on the magnitude of the orbital floor defects, models were allocated to the classes defined by Jaquiéry.

Models were imported into the software 3-Matic (Materialise, Leuven, BE) and the orbital floor defects were outlined by drawing a curve around the boundaries of the fracture (Fig. 2a). Within the same curve, a digital reconstruction of the orbital floor was simulated using spline-based methods, which enabled us to recreate the continuity of the interrupted surface. The digital reconstruction of the orbital floor was subsequently exported as a reference template to model a surgical guide (Fig. 2b). The guide was designed to be slightly larger than the orbital defect in order to provide a stable support for the graft. A handle was modelled on the guide to facilitate its positioning using surgical instruments. The surgical guide was exported as an STL (standard tessellation language) file

Table 2
Classification of orbital floor fractures according to Jaquiéry. The examples for class II and class III related to virtual reconstructions from our series.

Class	Description	Example from our case series
I	defect of the orbital floor or the medial wall, 1–2 cm^2	The protocol for endoscopic computer-guided surgical recon-struction does not apply to class I defects, which do not necessitate graft insertion
II	defect of the orbital floor and/or of the medial wall >2 cm^2 with preservation of the bony ledge at the medial margin of the infraorbital fissure	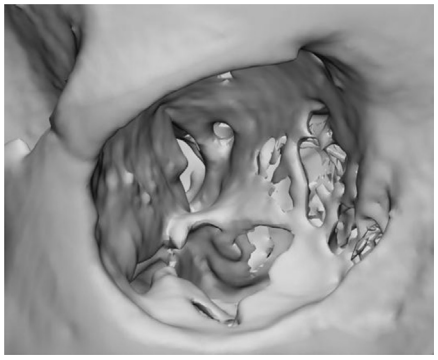
III	defect of the orbital floor and/or of the medial wall >2 cm^2 without preservation of the bony ledge of infraorbital fissure	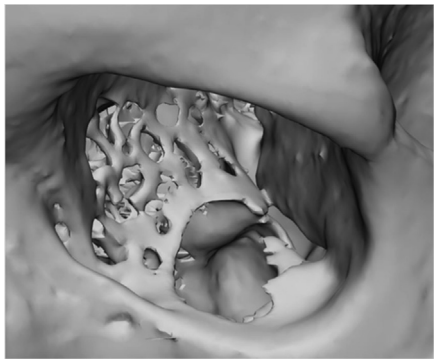
IV	defect of the entire orbital floor and the medial wall	Were excluded from the presented protocol because medial wall is not reachable using transantral endoscopy without performing removal of ethmoid boner
V	same as IV, with extension to the orbital roof	Were excluded from the presented protocol due to the involvement of the orbital roof

and 3D printed using a Form 2 (Formlabs, Somerville, MA, USA) stereolithographic 3D printer (Fig. 2c).

The source of bone graft was chosen according to Jaquiery's classification: for a class II defect the maxillary sinus bone represented a suitable choice, while for larger defects, such as class III, a larger donor area was preferred, such as the iliac crest. Finally, the transposition of the chosen graft onto the fracture site was simulated to evaluate the reciprocal compatibility.

2.3. Surgery

All surgeries were performed under general anesthesia using an intraoral approach. A 3 cm vestibular incision was made in the gingivobuccal sulcus to gain access to the anterior wall of the maxillary sinus. The surgical guide was applied to the maxillary bone surface, and a window was sculpted to match the orbital wall defect (Fig. 3a, b). Using Piezosurgery (Mecron, Carasco, Italy), a maxillary bone cut was performed to introduce the endoscope into the endosinusal space and view the fractured orbital floor from the bottom. The resulting excised bone dowel was then prepared to reconstruct the orbital floor for class II defects. For larger defects, typically >2 cm, the iliac crest was chosen as wider donor area. Thus, the premodelled surgical guide can be applied to the bone surface of the appropriate donor area, allowing the surgeon to harvest an optimally sized graft that matches the size and orientation of the orbital floor defect.

0-degree and 30-degree sinus endoscopes were introduced into the maxillary antrum for the transmaxillary inspection of herniated orbital content, maxillary sinus ostium, and infraorbital nerve. Using a periosteal elevator, herniated orbital fat was reduced into the orbital cavity with gentle pressure. Especially in cases of older fractures, meticulous detachment of fibrous tissue from the fracture rim was necessary in order to free the entrapped tissue and expose the fracture margins. During these phases, care was taken to avoid injuries to the infraorbital nerve and the inferior rectus muscle.

In cases with a comminuted orbital floor fracture, bone fragments were removed so that they would not project into the orbit.

The premodelled bone graft was inserted through the maxillary sinus window and pulled upwards until its peripheral edge could accommodate the margins of the fracture and achieve support for the orbital content (Fig. 3c). A biocollagen membrane was positioned over the maxillary opening and stabilized with bone-anchored sutures, and the mucogingival junction was tightly sutured.

2.4. Evaluation of accuracy in graft positioning

The protocol included the evaluation of accuracy by comparing the planned and achieved reconstruction of the orbital floor. Patients underwent a high-resolution CT scan 48 h after the operation and accurate segmentation was performed. The postoperative CT mesh was aligned to the preoperative entity using a global alignment function based on the iterative closest point algorithm. Once models were spatially coincident, bone graft was isolated from the postoperative CT scan by subtracting the preoperative CT mesh, containing the orbital defect, from the postoperative CT mesh.

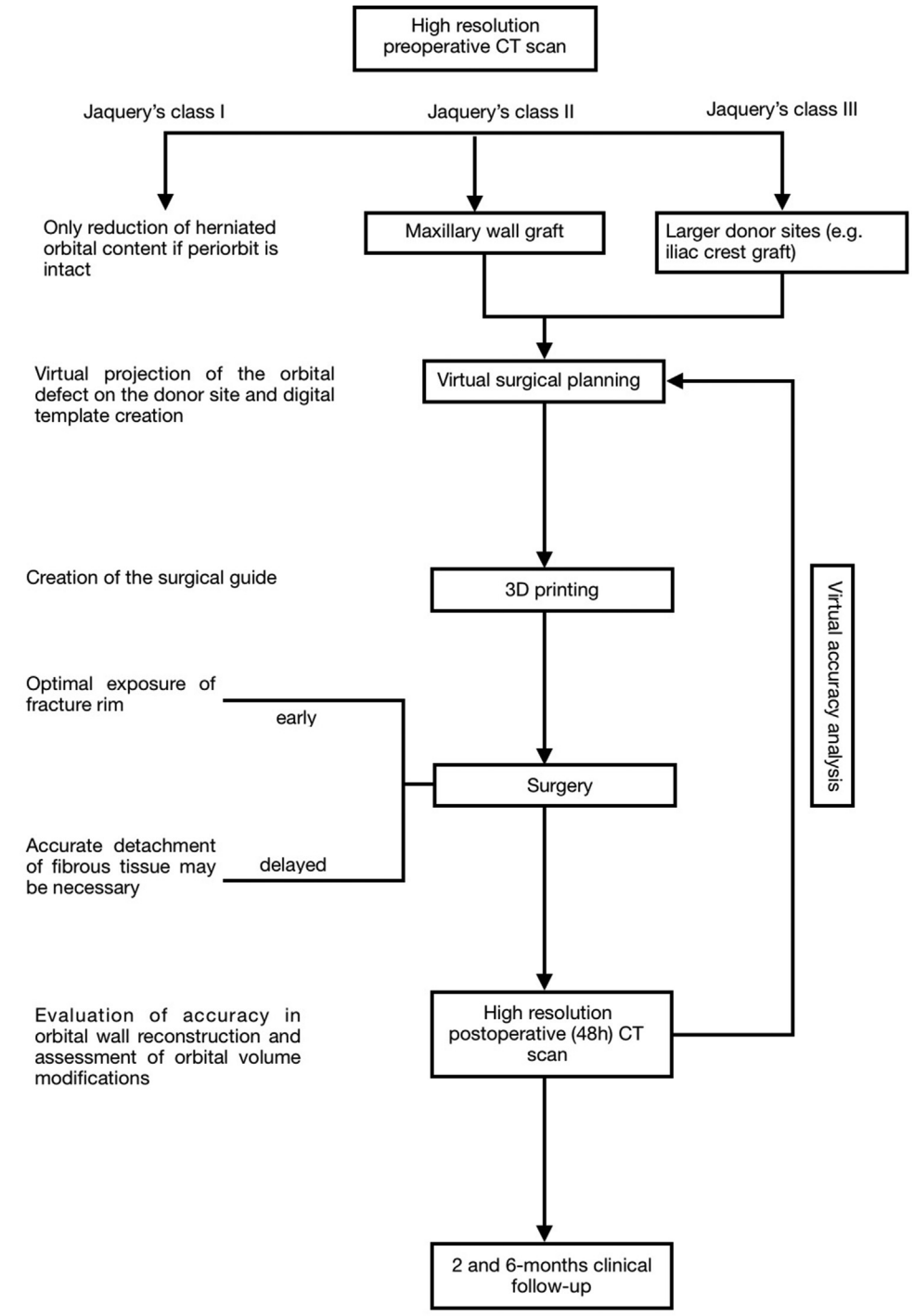

Fig. 1. Workflow for endoscopic, computer-guided repair of internal orbital floor fractures.

In order to estimate the accuracy of orbital floor reconstruction, a surface deviation analysis based on averaged Euclidean distances was performed between the planned and postoperative graft models. The resulting color map provided a visual representation of the overall accuracy in orbital floor reconstruction using a tolerance value of 1 mm (Fig. 4). Calculation of the root mean square error (RMSE) provided a numerical index describing the averaged discrepancy value between the planned and achieved reconstructions.

An additional evaluation was carried out concerning the differences in orientation between the planned and achieved reconstructions. In order to make measurements comparable between multiple patients, a common reference system was used for each pair of aligned entities, based on the model originally proposed by Schreurs et al., (2016). In our study, rotations were defined by measuring the angles between the major longitudinal axes of the planned and achieved graft

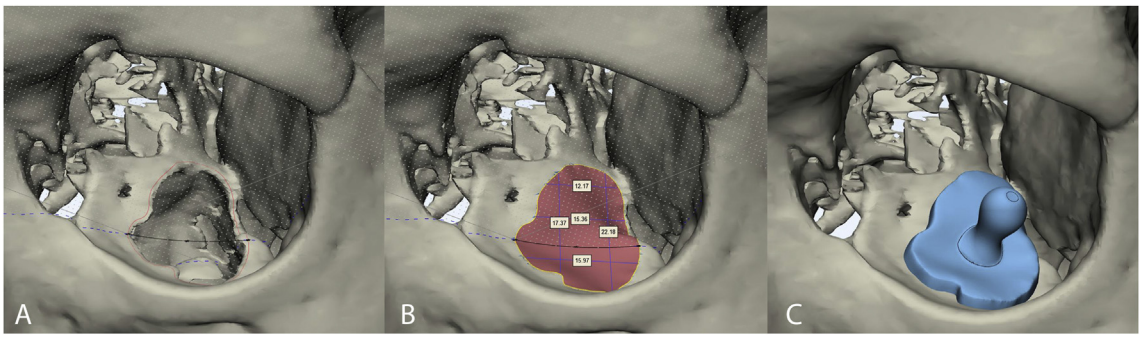

Fig. 2. Virtual surgical planning in orbital floor reconstruction. A) A curve is drawn to outline the defect. The curve is slightly larger than the size of the defect to facilitate accommodation of the graft onto the fracture rim. B) Virtual reconstruction of the orbital floor is performed independently of the contralateral orbit. A spline (black curve) is interpolated with the outline curve to recreate the virtual floor. Measurements are performed to verify the size of the graft for intraoperative use. C) The surgical guide is modelled on the virtual reconstruction of the orbital floor.

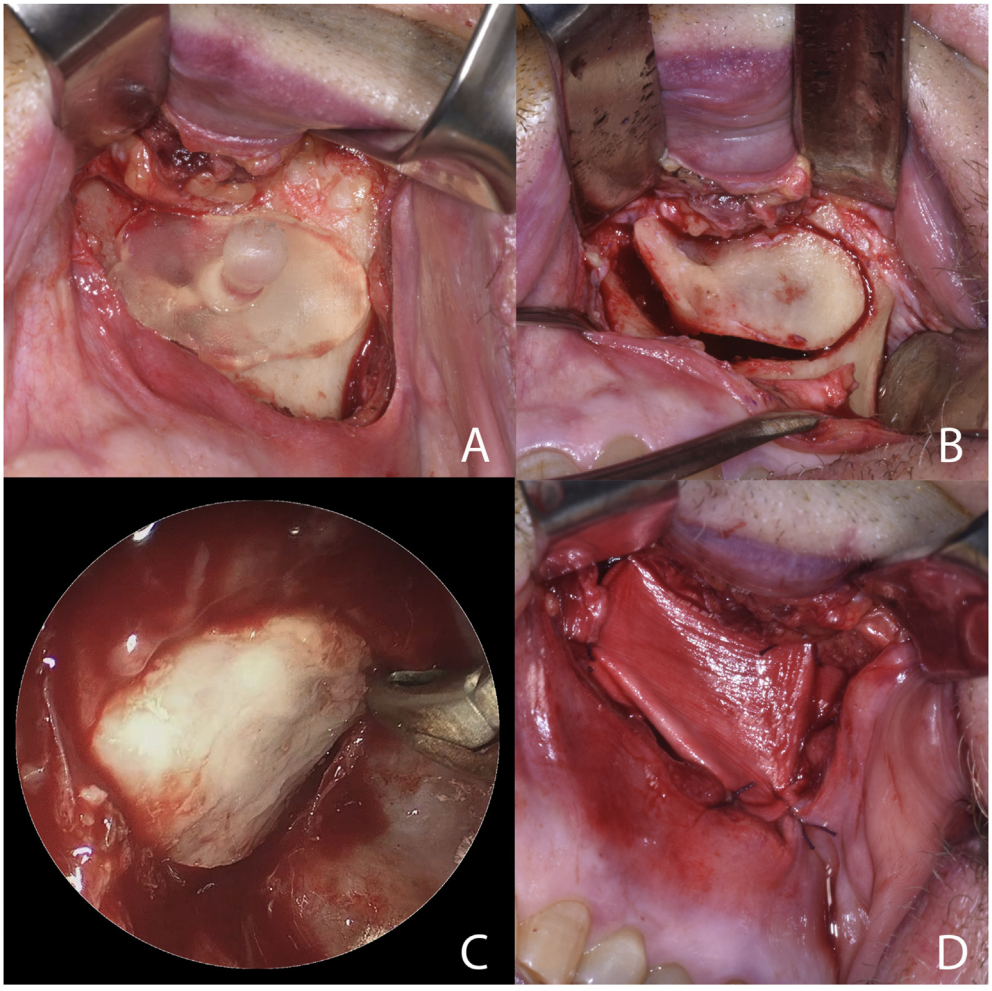

Fig. 3. A) The surgical guide is positioned over the anterior wall of the maxillary sinus to sculpt the window for the endosinusal space. B) The bone fragment is removed and used to reconstruct the orbital floor for class II or class III defects, depending on the size of the maxilla. C) Endoscopic view, showing the correct positioning of the graft and reconstruction of the orbital floor. D) Bone-anchored sutures are used to stabilize biocollagen membrane over the maxillary defect.

positions, based on their orthogonal projection on XY (horizontal), ZY (coronal) and ZX (parasagittal) planes. Such analysis allowed subdivision of the overall rotational differences into single components (Fig. 5).

3. Results

The extent of each orbital floor defect was measured on the CT scan and virtual 3D models and classified according to Jaquiéry

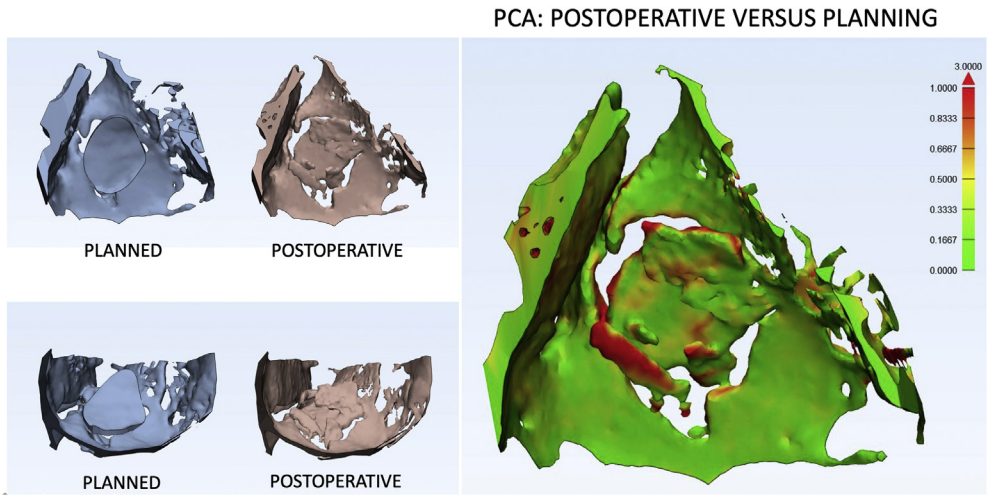

Fig. 4. Comparison of planned and achieved orbital floor reconstruction, and color-coded distance map used to quantify size difference between virtual and real grafts.

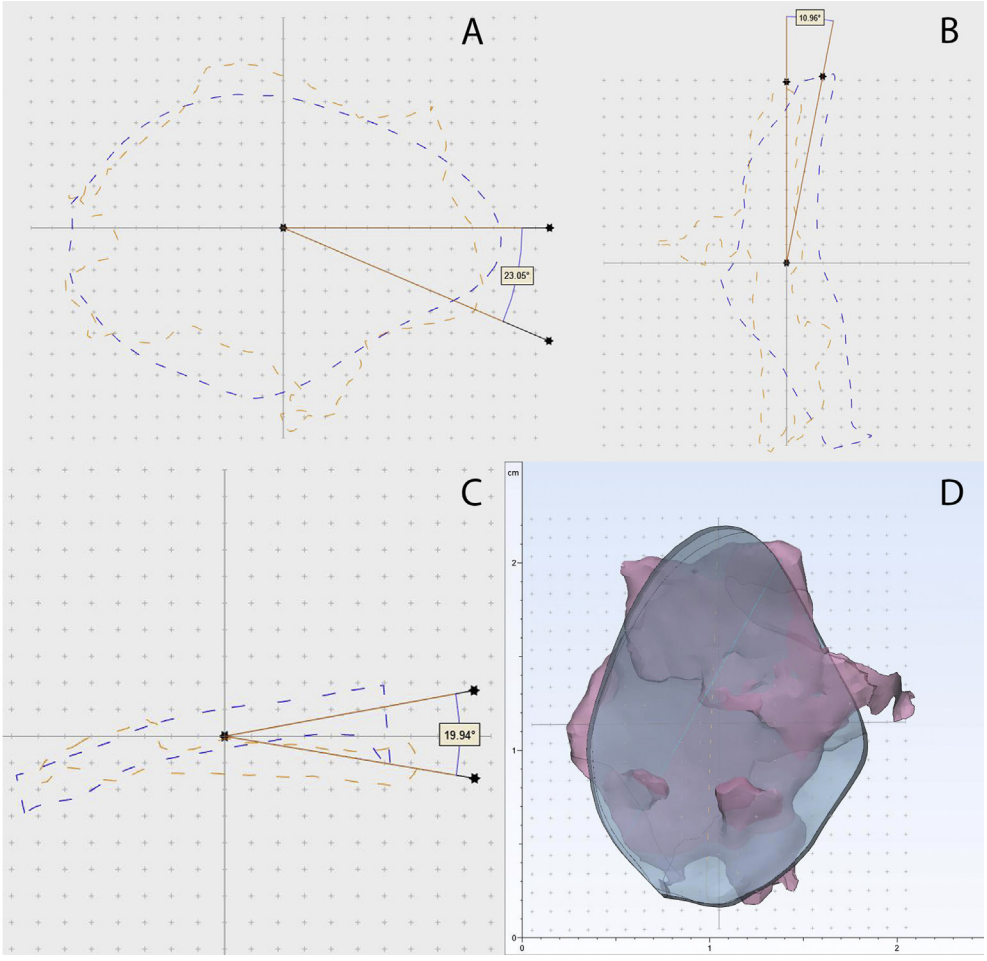

Fig. 5. Evaluation of graft orientation in orthographic projections. Planned graft is represented as a blue dashed line, while real graft is represented as an orange dashed line. A) XY (horizontal) plane; B) ZX (parasagittal) plane; C) ZY (coronal) plane; D) overlap of planned and achieved graft orientation. The reference system was created according to Schreurs at el (Schreurs et al., 2016).

et al., resulting in seven class II defects, four class III defects, and three class III defects with minimal involvement of the inferior aspect of the medial orbital wall.

All procedures were uneventful. All fractures were approached via a transantral endoscopic approach and surgical repair of each blowout fracture was performed using autologous bone graft. Mild infraorbitary nerve paresthesia was observed in two patients.

Preoperative diplopia assessed by a Hess chart was present in 12 patients preoperatively. After surgery, persistence of diplopia

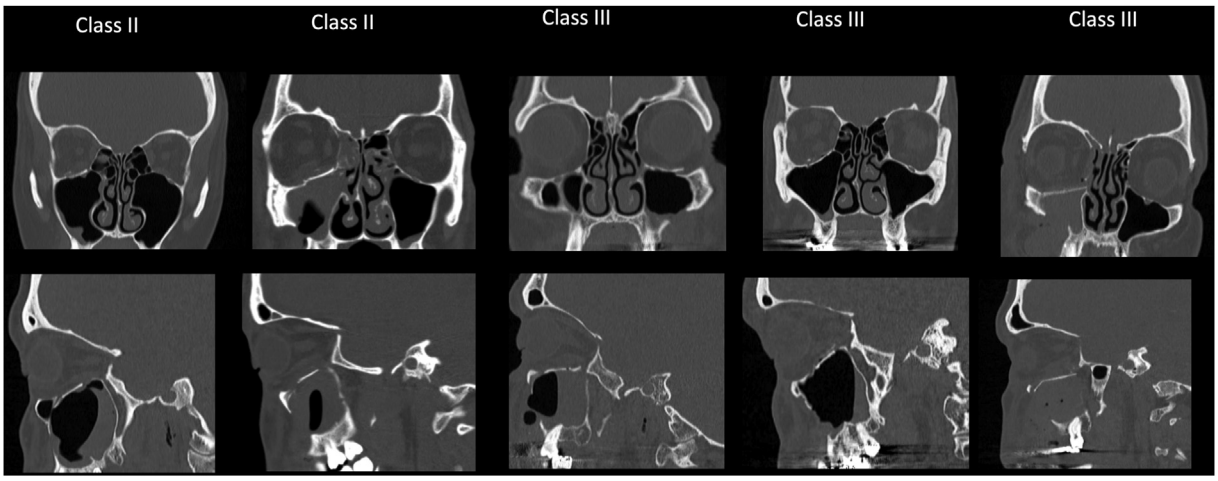

Fig. 6. Examples of postoperative results assessed by CT scan, using the most representative defects for each class taken from our series of patients.

Fig. 7. Comparison of the preoperative appearance of one patient with minimal enophthalmos with the postoperative clinical outcome.

was observed in only one patient. All cases of preoperative enophthalmos achieved visibly symmetric eyeball projection after surgery. Hertel exophthalmometry was used to measure the correction of eye globe horizontal displacement, namely enophthalmos correction. Enophthalmos was recorded as a negative deviation and exophthalmos was recorded as a positive deviation. Hertel scale measurements showed enophthalmos reduction from an average value of −0.92 mm preoperatively to −0.10 mm postoperatively.

Postoperative CT scans showed accurate reconstruction of the orbital floor shape, especially in sagittal and coronal views (Fig. 6) (see Fig. 7).

Table 3
Results of virtual analysis.

Patient	Jaquiéry's class	Mean error (mm)	SD (mm)	RMSE (mm)	XY deviation (°)	ZX deviation (°)	ZY deviation (°)
1	II	0.52	0.49	0.80	37.1	8.2	15.8
2	II	0.41	0.56	0.71	20.2	13.4	18.7
3	II	0.23	0.34	0.65	18.7	9.7	24.9
4	III	0.58	0.71	0.89	35.6	8.5	19.6
5	III	0.70	0.81	0.94	20.9	24.4	25.8
6	III	0.32	0.43	0.62	33.3	21.6	17.3
7	II	0.21	0.32	0.42	18.4	6.2	20.6
8	II	0.34	0.49	0.75	10.3	14.2	15.3
9	III	0.79	0.88	0.99	28.1	14.8	18.7
10	III	0.17	0.33	0.49	11.5	7.3	10.8
11	III	0.92	1.15	1.21	29.7	8.8	25.5
12	II	0.22	0.61	0.76	17.2	3.5	17.4
13	III	0.31	0.41	0.62	16.7	6.6	18.2
14	II	0.30	0.59	0.23	25.7	5.4	30.0
	Average	0.43	0.58	0.72	23.1	10.9	19.9

Virtual superimposition of planned and achieved reconstruction models allowed for a qualitative comparison of graft positioning. To quantify the difference in size between the postoperative graft and its planned counterpart, PCA and calculation of RMSE were performed. For all patients, average mean error was 0.43 mm (SD = 0.58) and RMSE was 0.72 mm. In all cases, except for one class III with minimal involvement of the medial orbital wall patient, RMSE was <1 mm, therefore indicating that orbital floor reconstruction was performed with an error margin inferior to 1 mm.

Evaluation of orientation showed an average rotational deviation of 23.1° for the XY (horizontal) plane, 10.9° for the ZX (parasagittal) plane, and 19.9° for the ZY (coronal) plane, confirming acceptable reproducibility for all patients. Results of the accuracy measurements are reported for each patient in Table 3.

4. Discussion

The purpose of this study was to introduce a protocol for the endoscopic management of internal orbital fractures, with the guidance provided by virtual reality surgical planning and 3D-printed surgical guides.

The transantral approach represents a reliable choice for the inspection and treatment of internal orbital floor fractures. It is performed intraorally and does not involve external incisions or visible scars. Additionally, technological improvements have made the transantral endoscopic approach an appropriate choice for direct visualization of orbital floor fracture, allowing the precise assessment of size, orientation, and need for repair (Persons and Wong, 2002). The accurate visualization provided by endoscopy is essential because intraoperative orbital fat prolapse can hinder visualization of the posterior aspect of the orbit. As a result, inaccurate reconstruction of the orbital floor, postoperative enophthalmos, and extraocular muscle entrapment can occur.

Transantral endoscopy allows the surgeon to safely reduce prolapsed orbital content within the orbital cavity and remove bony fragments (Kim et al., 2012). However, caution should be used to prevent entrapment of unreduced orbital content, and positioning of bone fragments should be performed without traumatizing the infraorbital nerve (Strong, 2006).

Another hazardous complication related to the treatment of orbital fractures is the occurrence of intraorbital haematoma. We consider that the wide opening on the anterior maxillary wall required by the transantral approach provides straightforward access to the bone graft, which can be promptly removed to achieve decompression of the haematoma. Consequently, evacuation of the haematoma can be achieved through the maxillary sinus, without any delay. If required, external incisions can also be performed to release the haematoma, including lateral canthotomy or inferior cantholysis (Brucoli et al., 2012). It is also worth mentioning that, compared with traditional transcutaneous routes, the transmaxillary approach further lowers the risk of damaging intraorbital vascular structures, since reduction of the herniated orbital content is achieved from the bottom and surgical instruments do not enter the orbital contents.

The choice of method for supporting the orbital floor after elevation of the orbital contents remains controversial. Some authors described the use of autogenous bone, titanium mesh, or a resorbable plate to reconstruct the orbital floor defect after transmaxillary reduction.

A feature of the endoscopic transantral approach is the possibility to harvest the graft and access the orbital floor in a single step, avoiding placement of alloplastic materials. In 1966, Kaye described the use of bone from the anterior wall of the maxillary antrum (Kaye, 1966); however, such techniques received relatively little recognition in the literature. There are distinct advantages of using maxillary antral bone, with many authors considering bone autografts to be the material of choice for bone tissue repair (Schlickewei and Schlickewei, 2007). In particular, antral bone graft has been shown to be particularly suitable for repairing the orbital floor because it avoids additional incisions and decreases the surgical time required to harvest and model the graft, while at the same time eliminating donor site morbidity. However, traditional indications for orbital floor reconstruction using antral bone graft have been applied to small defects, and in our protocol are limited to class II defects. For larger, class III defects, the transantral insertion of different bone autografts might be considered, including partial-thickness iliac crest or calvaria grafts, representing an alternative to the insertion of foreign materials, such as titanium meshes or Medpor implants.

Orbital reconstruction is challenging because of the high level of unpredictability. Especially when endoscopically positioning bone grafts, it is of paramount importance that the graft has the exact shape and size to suit the orbital defect. A subsized graft might be not supported by the fracture rim and consequently collapse inside the maxillary antrum, whereas an oversized graft might not pass through the orbital floor opening.

Since the early 2000s, surgery has taken advantage of computer-assisted design/computer-assisted manufacturing (CAD/CAM) methods, which have developed dramatically over recent years, leading to a remarkable improvements in the management of deformities in the orbital region (Scolozzi, 2017). Historically, mirroring of the contralateral healthy orbit has been commonly used to perform a virtual reconstruction of the orbital defect and design customized implants. Unfortunately, the main pitfall of such technique is that the human skull is geometrically asymmetric and, consequently, the two orbits might differ consistently. Therefore, when performing orbital floor reconstruction, we adopted spline interpolation techniques, enabling us to fill orbital defects using the surrounding healthy bony structures as a reference, as described by Vehmeijer et al., (2016). Additionally, virtual reconstruction of the orbital floor serves as a base on which to model a surgical guide, whose boundaries are identified by the perimeter of the orbital floor defect. The guide is designed slightly larger than the outline of the defect, allowing the harvesting of a relatively oversized graft, which fits over the orbital defect and is supported by the outline of the fracture. The guide is designed to simultaneously provide access to the maxillary sinus and shape an antral bone graft, acting as an all-in-one surgical guide (Tel et al., 2018), but it might be used likewise to model a different graft, such as a calvarial graft or an iliac crest graft.

The geometry of the reconstructed orbital floor might influence adverse clinical outcomes, such as enophthalmos and hypoglobus .

Traditionally, accuracy in reconstructing the orbital floor was evaluated by carrying out a postoperative, thin-sliced CT scan and then performing quantitative error assessment by tracing linear distances between the graft position and the contralateral mirrored orbit, which was set as the reference (Metzger et al., 2007). However, such analysis was hampered by the false assumption of symmetry between the affected and unaffected orbits, and the choice of points and CT slices with which to perform the measurements was arbitrary (Schreurs et al., 2016). Instead, color-coded distance maps are advisable for quantitative assessment of the graft position and to eliminate errors originating from the selection of the measurement points.

Our protocol introduces specific 3D analysis for the assessment of discrepancies between planned and postoperative reconstruction, in which the orbital floor is isolated and the achieved reconstruction is compared with its planned counterpart. A quantitative evaluation is provided that includes mean

error, standard deviation, and RMSE, the latter representing the average of Euclidean distances between planned and achieved orbital floor reconstruction. Next, superimposition of isolated graft models allows an estimation of graft rotational deviation by comparing the achieved graft position with the ideally planned orientation.

As with all techniques, repair of orbital floor fractures using the transantral endoscopy and virtual surgical planning described in this protocol has its own disadvantages. First and foremost, it requires investment in certified medical software and 3D printers, as well as expertise in virtual surgical planning, which might require the presence of specifically trained surgeons with proficiency in CAD-CAM technologies. However, alloplastic materials, such as titanium meshes and ceramic implants, involve dramatically superior costs, require longer times for production, and cannot be positioned endoscopically. The surgical guide printed in this protocol has a negligible cost and can be rapidly available if the center has a 3D laboratory. Endoscopic approaches might require longer operating times, especially for surgeons new to the technique, but increased experience in this technique has been shown to reduce surgical duration.

5. Conclusion

In this protocol we present an updated protocol for the endoscopic management of class II and class III internal orbital floor fractures, using virtual reality and 3D printing. The main innovations include use of a surgical guide to perform one-step access to the endosinusal space and graft modeling, context-driven reconstruction of the orbital defect based on spline interpolation instead of orbital mirroring, and evaluation of accuracy between individually aligned planned and positioned grafts. Our experience in orbital reconstruction shows that the use of CAD-CAM by surgeons performed within a 3D printing lab can shorten presurgical planning, facilitate intraoperative maneuvers, and increase accuracy of reconstruction.

5.1. Special Remarks

This work was presented at the 21st congress of the Italian Society for Maxillo-Facial Surgery and won the Costantino Giardino prize for the scientific innovation.

References

Ahmad Nasir S, Ramli R, Abd Jabar N: Predictors of enophthalmos among adult patients with pure orbital blowout fractures. Plos One 13(10): e0204946, 2018

Beigi B, Khandwala M, Gupta D: Management of pure orbital floor fractures: a proposed protocol to prevent unnecessary or early surgery. Orbit 33(5): 336–342, 2014

Brucoli M, Arcuri F, Giarda M, Benech R, Benech A: Surgical management of post-traumatic intraorbital hematoma. J Craniofac Surg 23(1): e58–e61, 2012

Damgaard OE, Larsen CG, Felding UA, Toft PB, von Buchwald C: Surgical timing of the orbital 'blowout' fracture: a systematic review and meta-analysis. Otolaryngol Head Neck Surg 155(3): 387–390, 2016

Farwell DG, Strong EB: Endoscopic repair of orbital floor fractures. Otolaryngol Clin N Am 40(2): 319–328, 2007

Jaquiéry C, Aeppli C, Cornelius P, Palmowsky A, Kunz C, Hammer B: Reconstruction of orbital wall defects: critical review of 72 patients. Int J Oral Maxillofac Surg 36(3): 193–199, 2007

Kaye BL: Orbital floor repair with antral wall bone grafts. Plast Reconstr Surg 37(1): 62–65, 1966

Kim K, Song K, Choi S, Bae Y, Choi C, Oh H, et al: Endoscopic transnasal approach for the treatment of isolated medial orbital blow-out fractures: a prospective study of preoperative and postoperative orbital volume change. Ann Plast Surg 68(2): 161–165, 2012

Kwon JH, Kim JG, Moon JH, Cho JH: Clinical analysis of surgical approaches for orbital floor fractures. Arch Facial Plast Surg 10(1), 2008

Mazock JB, Schow SR, Triplett RG: Evaluation of ocular changes secondary to blowout fractures. J Oral Maxillofac Surg 62(10): 1298–1302, 2004

Metzger MC, Hohlweg-Majert B, Schön R, Teschner M, Gellrich NC, Schmelzeisen R, et al: Verification of clinical precision after computer-aided reconstruction in craniomaxillofacial surgery. Oral Surg, Oral Med, Oral Pathol, Oral Radiol, Endodontology 104(4): e1–e10, 2007

Nahlieli O, Bar-Droma E, Zagury A, Turner MD, Yoffe B, Shacham R, et al: Endoscopic intraoral plating of orbital floor fractures. J Oral Maxillofac Surg 65(9): 1751–1757, 2007

Persons BL, Wong GB: Transantral endoscopic orbital floor repair using resorbable plate. J Craniofac Surg 13(3): 483–488, 2002 discussion 488–89

Sanno T, Tahara S, Nomura T, Hashikawa K: Endoscopic endonasal reduction for blowout fracture of the medial orbital wall. Plast Reconstr Surg 112(5): 1228–1237, 2003

Schlickewei W, Schlickewei C: The use of bone substitutes in the treatment of bone defects — the clinical view and history. Macromol Symp 253(1): 10–23, 2007

Schreurs R, Dubois L, Becking AG, Maal TJ: Quantitative assessment of orbital implant position — a proof of concept. In: Elsalanty ME (ed.), Plos One 11(3): e0150162, 2016

Scolozzi P: Applications of 3D orbital computer-assisted surgery (CAS). J Stomatol, Oral Maxillofac Surg 118(4): 217–223, 2017

Strong EB: Endoscopic repair of orbital blow-out fractures. Oper Tech Otolaryngol Head Neck Surg 17(3): 201–209, 2006

Strong EB, Kenneth KK, Rodney CD: Endoscopic approach to orbital blowout fracture repair. Otolaryngol Head Neck Surg 131(5): 683–695, 2004

Tel A, Costa F, Sembronio S, Lazzarotto A, Robiony M: All-in-one surgical guide: a new method for cranial vault resection and reconstruction. J Cranio-Maxillofacial Surg 46(6): 967–973, 2018

Vehmeijer M, van Eijnatten M, Liberton N, Wolff J: A novel method of orbital floor reconstruction using virtual planning, 3-dimensional printing, and autologous bone. J Oral Maxillofac Surg 74(8): 1608–1612, 2016